AIAA JOURNAL
Vol. 34, No. 9, September 1996

Two-Dimensional Model for Spark Discharge Simulation in Air

M. Akram*
Lund Institute of Technology, Lund S-221 00, Sweden

A two-dimensional model simulating the hydrodynamic behavior of the plasma produced by an ultrafast pin-to-pin electrical spark discharge in air is presented. The plasma is considered to behave like nonviscous, single-substance, nonpolar, heat-conducting fluid. It is assumed that local thermodynamic equilibrium prevails within the domain of calculation. The energy input is determined by a prescribed electric current, coupled with a computation of plasma conductivity. Radiative losses from the domain also are considered. The model employs an equation of state for air that includes the effects of vibration, ionization, and dissociation energies at high temperature. Governing equations are solved numerically using the MacCormack time-splitting technique. An explicit artificial viscosity term is introduced into the equations, and flux-corrected transport is used as a postshock oscillation damper. The results show that the hydrodynamic effects and electrode geometry are responsible for the formation of a torus-like plasma kernel.

Nomenclature

A_0, A_1, A_2	= extents to which dissociation, first ionization, and second ionization have proceeded
$\boldsymbol{B}$	= magnetic intensity
$\boldsymbol{b}$	= body force
C_0, C_1, C_2	= constants in the equations of state, depending on the statistical weights of the particles in the plasma
c	= speed of light
c_0	= local speed of sound in a medium
$\boldsymbol{E}$	= electric field
e	= total (internal + kinetic) energy density
h	= Planck's constant
$\boldsymbol{h}$	= heat flux vector, $-\kappa \operatorname{grad}\theta$
I_0, I_1, I_2	= dissociation, first ionization, and second ionization energies, respectively
$\boldsymbol{j}$	= electric current
K_b	= absorption coefficient
k	= Boltzmann's constant
$\boldsymbol{m}$	= linear momentum density with components (m_r, m_ϕ, m_z), such that $m_r = \rho u$, etc.
p	= pressure
$\Re$	= gas constant
s_J	= joule heating
s_R	= radiative losses
$\boldsymbol{T}$	= Cauchy stress tensor
$\boldsymbol{v}$	= velocity field with components u, v, w in cylindrical coordinates
$\boldsymbol{v}_e$	= electron velocity
ε	= specific internal energy
θ	= absolute temperature
θ_v	= vibrational temperature
κ	= thermal conductivity
σ	= electrical conductivity
$\mathbf{1}$	= unit tensor

Introduction

THE increasing pollution poses a threat to the survival of living creatures on our beloved planet Earth. To reduce emission of unwanted gases from the internal combustion engine, it is required to run it on reasonably lean fuel mixtures, which is not possible with the conventional ignition systems. Thus, for better understanding of spark ignition of gas mixtures, it is important to study the evolution of flow in the early phase of the electrical discharge, especially for ultrafast ignition systems. These systems are designed to supply comparatively higher power into the mixtures. In a typical system, the electrical current rises to some hundreds of amperes in about some tens of nanoseconds after breakdown and then drops down to milliamperes in about a few hundreds of nanoseconds.

During the past decade, study has focused on the evolution of the plasma kernel from a spark discharge. The hypothesis put forward by Chomiak[1] that the entraining cloud that propagates from a conventional axial spark can itself be considered as a hydrodynamic puff, has been supported by the studies of Haley and Smy.[2] Here the blast-wave theory has been used to explain the puff, and the flow pattern is observed with schlieren photographs. The evolution of the plasma kernel for short-duration sparks in an inert gas is presented, where the expansion of a hot plasma kernel into cold gas is modeled by equations of gasdynamics.[3] The influence of electrode configuration is studied and supported by experiments.

It is demanding to study the evolution of a flowfield just after the breakdown and while the energy is still being put into the system. Because the electrical properties of hydrocarbons are not well known, air has been chosen for this study. The breakdown of the gas occurs in about 1 ns after the current is switched on and in about 10 ns an electrically conducting channel of about 40-μm radius and temperature as high as 60,000 K is formed.[4] In the work reported here, the breakdown stage is assumed to be in the form of a thin plasma channel in which local thermodynamic equilibrium can be assumed. The plasma is assumed to be a neutral, single-substance material with homogeneous properties. This paper is the two-dimensional extension of work already presented,[5] where a one-dimensional cylindrically symmetric, transient, Lagrangian hydrodynamic model is given for the spark-discharge simulation. For one-dimensional cylindrical symmetry, one assumes the spark gap to be infinitely long, which is far from reality considering the study of the laboratory-scale sparks. For such studies, the so-called edge effects cannot be ignored, and at least a two-dimensional model is required for adequate understanding of the phenomena. By assuming an axial symmetry in cylindrical coordinates, a two-dimensional model is formulated and solved numerically.

Because the advantages of working in Lagrangian description diminish when we extend our model to two space dimensions, the Eulerian description of the fluid motion is adopted. The assumptions made regarding the physical model described previously[5] and given in the next section remain the same except the symmetry condition. Instead of cylindrical symmetry, an axial symmetry is assumed. This means that all dependent variables are functions of r and z (radial and axial coordinates, respectively). Electrode geometry is introduced and the effect of heat transfer to electrodes and the changes in flowfield are studied. Two types of electrode pins are studied, namely, cylindrical with tapered tip (case I) and cylindrical with plane tip (case II).

Received March 2, 1995; revision received April 1, 1996; accepted for publication May 17, 1996. Copyright © 1996 by the American Institute of Aeronautics and Astronautics, Inc. All rights reserved.

*Graduate Student, Department of Combustion Physics, Box 118.

Initially, it is assumed that a cylindrically symmetric breakdown channel is formed, thus introducing the breakdown phenomena into the initial condition for this model. Different initial conditions regarding the size, pressure, and temperature of breakdown channel also are studied.

Physical Model

The theoretical model presented here is based on the following assumptions:

1) No body forces are present, i.e., mechanical or electromagnetic.

2) Single-substance material, i.e., all constituents of the plasma, behave identically as far as their thermomechanical response is concerned.

3) Axial symmetry in cylindrical coordinates (r, ϕ, z), i.e., flow-field is independent of ϕ coordinate.

4) Conditions for local thermodynamic equilibrium (LTE) prevail throughout the time domain of computation.

5) The magnetic field generated by the electrical current passing through the plasma is negligible.

Assumptions 2 and 4 are not totally justified. The presence of an electric field influences the equilibration time; the difference in electron and ion/neutral temperatures decreases with increasing ion/neutral temperature and electron density. In most of the sparks, this process of thermalization takes place in about 10 ns, and the plasma becomes a homogeneous mixture of different particles (electrons, ions, and neutrals) in which local thermodynamic equilibrium can be assumed.[4] Therefore, about 10 ns after the onset of spark, the further evolution can be studied without a substantial error.

Equations of Motion

The general equations governing the motion of a nonpolar single-substance continuum material, ignoring nonlocal effects and confining the role of electromagnetic influences only to joule heating, are as follows:

$$\dot{\rho} = -\rho \operatorname{div} \boldsymbol{v} \qquad \text{(conservation of mass)} \tag{1}$$

$$\rho \dot{\boldsymbol{v}} = \rho \boldsymbol{b} + \operatorname{div} \boldsymbol{T} \qquad \text{(balance of momentum)} \tag{2}$$

$$\boldsymbol{T} = \boldsymbol{T}^T \qquad \text{(balance of moment of momentum)} \tag{3}$$

$$\rho \dot{\varepsilon} = \operatorname{tr}(\boldsymbol{T}^T \operatorname{grad} \boldsymbol{v}) - \operatorname{div} \boldsymbol{h} + s_J + s_R \qquad \text{(balance of energy)} \tag{4}$$

Here, ρ is the mass density and T is Cauchy's stress tensor with components such that $\boldsymbol{T} = \boldsymbol{e}_j T_{jk} \boldsymbol{e}_k = T_{jk} \boldsymbol{e}_j \otimes \boldsymbol{e}_k$. The specific internal energy ε represents the energy stored internally in the body per unit mass and is a macroscopic reflection of things such as the chemical binding energy, the intermolecular energy, and the energy of molecular vibration; it also may include the dissociation and/or the ionization energy. Among the heat flux vector components (h_r, h_ϕ, h_z), h_r denotes the amount of heat per unit area per unit time that crosses a surface normal to the r axis in the increasing r direction; s_J is the heating source, s_R is the heating sink, and the superimposed dot over a variable stands for the material time derivative.

With the given assumptions, Eqs. (1), (2), and (4), using the symmetry property of stress tensor T [i.e., Eq. (3)], can be written in a so-called conservative form by introducing new variables, i.e., mass density ρ; linear momentum density m having components (m_r, m_ϕ, m_z), where, for example, $m_r = \rho u$; and $e - [e = \rho(\varepsilon + \frac{1}{2}\boldsymbol{v} \cdot \boldsymbol{v}]$ total (internal plus kinetic) energy density as primitive variables.

Mass conservation:

$$\frac{\partial \rho}{\partial t} + \frac{\partial m_r}{\partial r} + \frac{\partial m_z}{\partial z} + \frac{m_r}{r} = 0 \tag{5}$$

Balance of momentum:

$$\frac{\partial m_r}{\partial t} + \frac{\partial}{\partial r}\left(\frac{m_r^2}{\rho} - T_{rr}\right) + \frac{\partial}{\partial z}\left(\frac{m_r m_z}{\rho} - T_{rz}\right) + \frac{1}{r}\left(\frac{m_r^2}{\rho} - T_{rr} + T_{\phi\phi}\right) = 0 \tag{6}$$

$$\frac{\partial m_z}{\partial t} + \frac{\partial}{\partial r}\left(\frac{m_r m_z}{\rho} - T_{rz}\right) + \frac{\partial}{\partial z}\left(\frac{m_z^2}{\rho} - T_{zz}\right) + \frac{1}{r}\left(\frac{m_r m_z}{\rho} - T_{rz}\right) = 0 \tag{7}$$

Balance of energy:

$$\frac{\partial e}{\partial t} + \frac{\partial}{\partial r}\left\{\frac{1}{\rho}[m_r(e - T_{rr}) - m_z T_{rz}] + h_r\right\} + \frac{\partial}{\partial z}\left\{\frac{1}{\rho}[m_z(e - T_{zz}) - m_r T_{rz}] + h_z\right\} + \frac{1}{r}\left[\frac{m_r}{\rho}(e - T_{rr}) - \frac{m_z}{\rho} T_{rz} + h_r\right] - s_J - s_R = 0 \tag{8}$$

Equations (5–8) are to be supplemented by the constitutive assumptions for the Cauchy stress tensor and the heat flux vector. Moreover, explicit definitions for the terms s_J and s_R also are required. Finally, thermal and caloric equations of state for real air/gas are added, and the system is complete for solution.

Constitutive Assumptions

The constitutive assumptions for stress tensor T and heat flux vector $\boldsymbol{h}$ are taken to be

$$\boldsymbol{T} = -p\boldsymbol{1} \tag{9}$$

$$\boldsymbol{h} = -\kappa \operatorname{grad} \theta \tag{10}$$

where p is hydrodynamic pressure and θ is absolute temperature.

It is well known that heat transfer by thermal conduction and momentum transfer by viscosity are of the same orders in a single-substance material.[6] Thus, ignoring one of these automatically means neglecting the other. In the case under consideration, there are free electrons that play an important role in the thermal conduction but has little effect in the momentum transport because of their very low mass as compared to ions and neutrals. Thus our constitutive assumption of introducing thermal conduction and ignoring viscosity is justified here.

The real air is replaced by a hypothetical diatomic gas; considering the contribution of vibrational degrees of freedom to the internal energy and taking the molecular weight, rotational moment of inertia, energies of dissociation, first and second ionization, and the statistical weights of the ground states (including low-lying excited states) of the molecular, atomic, and ionic species to be the weighted averages of the corresponding quantities for nitrogen and oxygen. This equation of state misrepresents air in the temperature range 3000–9000 K, because the dissociation energies of O_2 and N_2 are very different, but at temperatures above 10,000 K, the approximations made are much better, because the ionization potentials of nitrogen and oxygen are quite similar for temperature above 10,000 K. On the basis of these assumptions,[7] we write the equations of state used here.

Thermal equation of state:

$$p = \rho \Re \theta [1 + A_0 + 2(A_1 + A_2)] \tag{11}$$

Caloric equation of state:

$$\varepsilon = \Re\theta\left[\tfrac{1}{2}(5 + A_0) + 3(A_1 + A_2)\right] + A_0 I_0 + A_1 I_1 + A_2 I_2 \tag{12}$$

where

$$A_0 = 2\left[1 + (1 + 2B_0)^{\frac{1}{2}}\right]^{-1}$$

$$B_0 = C_0 \rho \theta^{-\frac{1}{2}}\left[1 - \exp(-\theta v/\theta)\right]^{-1} \exp(I_0/\Re\theta)$$

$$A_1 = 2\left[1 + (1 + 2B_1)^{\frac{1}{2}}\right]^{-1}, \quad B_1 = C_1 \rho \theta^{-\frac{3}{2}} \exp(I_1/2\Re\theta) \tag{13}$$

$$A_2 = 2\left[1 + 2B_2 + \left(1 + 6B_2 + B_2^2\right)^{\frac{1}{2}}\right]^{-1}$$

$$B_2 = C_2 \rho \theta^{-\frac{3}{2}} \exp(I_2/2\Re\theta)$$

Table 1 Values of constants

Parameter name	Value	Units
Gas constant $\Re$	2.880946×10^2	$JK^{-1}\,kg^{-1}$
Specific dissociation energy I_0	2.930557×10^7	Jkg^{-1}
Specific first ionization energy I_1	9.591766×10^7	Jkg^{-1}
Specific second ionization energy I_2	2.062056×10^8	Jkg^{-1}
Constant in Saha equation for dissociation C_0	4.817588×10^{-4}	$m^3K^{3/2}kg^{-1}$
Constant in Saha equation for first ionization C_1	1.101416×10^4	$m^3K^{3/2}kg^{-1}$
Constant in Saha equation for second ionization C_2	1.033965×10^4	$m^3K^{3/2}kg^{-1}$
Vibrational temperature θ_v	3150.0	K
Density of air ρ_0	1.172358	kgm^{-3}
Temperature θ_0	300.0	K
Pressure p_0	1.01325×10^5	Pa

In the above expressions, the A_i are the extents to which dissociation and ionization reactions have proceeded ($0 \le A_i \le 1$), the I_i are the specific energies of dissociation or ionization, θ_v is the vibrational temperature, and the C_i are constants dependent on the statistical weights, and so forth, of the respective particles. The values of all these constants used here are given in Table 1.

Electrical Power Input (Joule Heating)

The electrical power input to the gas is given by

$$s_J = (\boldsymbol{j} \cdot \boldsymbol{E}) \tag{14}$$

where $\boldsymbol{j}$ is the electric current and $\boldsymbol{E}$ is the electric field. The constitutive relation for the electric current $\boldsymbol{j}$ is given from the generalized Ohms law[8] and is

$$\boldsymbol{j} = \sigma(\boldsymbol{E} + \boldsymbol{v}_e \times \boldsymbol{B}) + \rho_e \boldsymbol{v}_e \tag{15}$$

where ρ_e is the excess charge density, σ is the electrical conductivity of the plasma, and $\boldsymbol{v}_e$ is the charge velocity field. Assuming the plasma to be electrically neutral and the magnetic field generated by the electric current to be negligibly small, we are left with

$$\boldsymbol{j} = \sigma \boldsymbol{E} \tag{16}$$

The electrical conductivity σ of the plasma [in the units $(\Omega m)^{-1}$] is given by[9]

$$\sigma = \frac{4.273 \times 10^{-8}(A_1 + A_2)\theta^{-\frac{1}{2}}}{2 \times 10^{-15}(1 - A_1) + A_1 a_i} \tag{17}$$

where the average electron–ion cross section a_i is

$$a_i = 2.8 \times 10^{-6}\theta^{-2}\left(\frac{A_1 + 3A_2}{A_1 + A_2}\right)^2 \times \log\left[\frac{1.727 \times 10^{-4}(A_1 + A_2)\theta}{(A_1 + 3A_2)(A_1\rho)^{\frac{1}{3}}}\right] \tag{18}$$

Using the prescribed (measured experimentally) electric current, the electric field can be calculated from Eqs. (16) and (17). Therefore, the electrical power input into the plasma through joule heating (in the units $Jm^{-3}s^{-1}$), with the further assumption that electrical current flows in the z direction only, is given by the relation

$$s_J = \sigma E_z^2 \tag{19}$$

Energy Transfer by Thermal Conduction

The mechanism of thermal conduction in a gas depends upon temperature; at low temperatures, energy transfer takes place via collisions between heavy particles, whereas for an ionized gas, conduction by electrons predominates. For molecular gases, still another process is important at intermediate temperatures—the transport of recombination energy across atom–molecule concentration gradients. To include all of these processes, the coefficient of thermal conductivity κ is considered to be the sum of 1) κ_e, the thermal conductivity by electrons; 2) κ_c, the magnitude of the contribution from the diffusion of the recombination energy; and 3) κ_0, the contribution of neutral particles. The thermal conductivity of the plasma (in the units $Jm^{-1}s^{-1}K^{-1}$) is assumed to be given by

$$\begin{aligned} \kappa &= \kappa_e + \kappa_c + \kappa_0 \\ \kappa_e &= 0.1488 \times 10^{-7}\sigma\theta \\ \kappa_c &= 2.2 \times 10^5 \rho \frac{dA_0}{d\theta} \\ \kappa_0 &= 1.0 \times 10^{-2}(1 - A_1)\theta^{\frac{1}{2}} \end{aligned} \tag{20}$$

Radiative Energy Transfer

Two types of radiative heat losses are considered here. Radiation energy loss in the long-wave region attributable to free–free transitions (bremsstrahlung, in the units $Jm^{-3}s^{-1}$) is given by

$$(s_R)_{ff} = -2.457 \times 10^{11}\theta^{\frac{1}{2}}A_1^2\left(\frac{A_1 + 3A_2}{A_1 + A_2}\right)^3 \tag{21}$$

The other loss term was obtained by assuming some absorption coefficient K_b, which was applied to the whole blackbody emission curve. Coefficient K_b is arbitrarily chosen such that the photon mean free path, referred to the gas density in the undisturbed atmosphere, is 1 cm, i.e.,

$$(K_b\rho_0)^{-1} = 1.0 \times 10^{-2}\ \text{m} \tag{22}$$

The radiative loss attributable to blackbody emission (in units $Jm^{-3}s^{-1}$) is then given by

$$(s_R)_b = -\frac{8\pi^5 k^4}{15h^3c^2}K_b\rho\theta^4 \tag{23}$$

The net rate of radiative energy loss is the sum of the above two terms:

$$s_R = (s_R)_{ff} + (s_R)_b \tag{24}$$

Numerical Solution

Using Eqs. (9) and (10), Eqs. (5–8) can be compactly written in the form of the following vector equation:

$$\frac{\partial U}{\partial t} + \frac{\partial G}{\partial r} + \frac{\partial H}{\partial z} + \Phi = 0 \tag{25}$$

where

$$U = [\rho, m_r, m_z, e]^T$$

$$G = \left[m_r, \left(m_r^2/\rho\right) + p, (m_r m_z/\rho), (m_r/\rho)(e + p) + h_r\right]^T$$

$$H = \left[m_z, (m_r m_z/\rho), \left(m_z^2/\rho\right) + p, (m_z/\rho)(e + p) + h_z\right]^T$$

$$\Phi = \left\{(m_r/r), \left(m_r^2/\rho_r\right), (m_r m_z/\rho_r), (1/r)[(m_r/\rho)(e + p) + h_r] - s_J - s_R\right\}^T$$

$$h_r \equiv -\kappa\frac{\partial\theta}{\partial r}; \qquad h_z \equiv -\kappa\frac{\partial\theta}{\partial z}$$

and s_J and s_R are defined by Eqs. (19) and (24), respectively.

Equation (25) is solved using the MacCormack time-splitting scheme.[10,11] The scheme is second-order accurate. An explicit artificial viscosity term of the type

$$S = a(\Delta r)^4\frac{\partial}{\partial r}\left[\frac{|u| + c_0}{4p}\left|\frac{\partial^2 p}{\partial r^2}\right|\frac{\partial U}{\partial r}\right] \tag{26}$$

for direction r and

$$\Sigma = a(\Delta z)^4 \frac{\partial}{\partial z}\left[\frac{|w| + c_0}{4p}\left|\frac{\partial^2 p}{\partial z^2}\right|\frac{\partial U}{\partial z}\right] \tag{27}$$

for direction z, which are equivalent to fourth-order diffusion and are introduced in the respective equations. In Eqs. (26) and (27), c_0 is the local speed of sound and $0 \le a \le 0.5$ is a stability factor (taken equal to 0.125 in all calculations reported here). Further, these terms have a very small magnitude except in the regions of pressure oscillations. Phoenical type of the flux corrected transport (FCT) algorithm is used for the better resolution of the shock wave and other steep gradients appearing in the flowfield.[12]

Computational Domain and the Mesh

The geometry of the system under consideration is illustrated in Fig. 1. L and M are the two metallic cylindrical electrodes with tapered facing ends (case I) and with plane facing ends (case II). The facing ends are considered to be flat here. In experimental setup it is difficult to get a symmetrical spark with this kind of pin and, in reality, some hemispherical-like curvature is necessary. This little abstraction facilitates the mesh generation. Because of axial symmetry the computational domain is reduced to $ABCDEE'D'C'B'A'$ in case I and to $ABDEE'D'B'A'$ in case II. The computational domain is divided into a square mesh. The angles ABC and $A'B'C'$ are assumed to be equal to $\frac{3}{4}\pi$, so that the subboundaries BC and $B'C'$ always fall on the grid points.

Domain of Computation and Initial Conditions

The electrode radius is taken equal to 0.5 mm. The domain of computation ranges from 10 ns to 40 μs in t, 0 to 6 mm in r, and -4.5 to 4.5 mm in z. The spark gap is taken to be 2 mm. The electrical current-time curve given by Borghese et al.[13] is used in these calculations and is given in Fig. 2. This curve is used to calculate the source term s_J throughout the computations. For initial condition, it is assumed that at 10 ns after switching on the electric current into

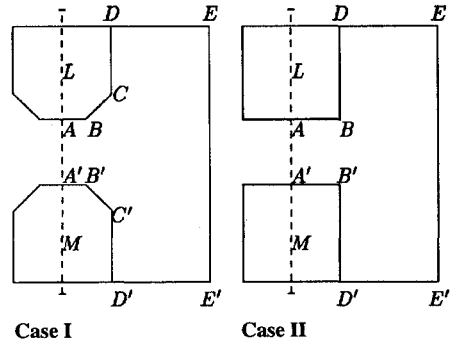

Fig. 1 Electrode geometry and the computational domain.

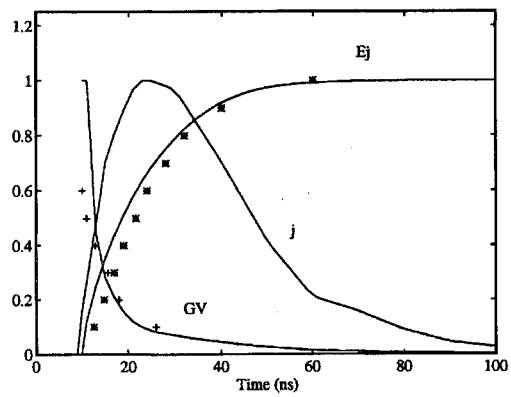

Fig. 2 Scaled waveforms vs time (ns): j = electric current taken from Ref. 13 (Max j = 385 A); GV = calculated gap voltage (max GV = 16 kV), + = experiment (max V = 12 kV); and Ej = calculated energy entering the gas (max Ej = 12 mJ), ∗ = experiment (max E = 14 mJ).

the spark circuit, a cylindrical breakdown channel of radius 0.05–0.1 mm is formed with temperature on its axis of symmetry equal to 7.5×10^3–15×10^3 K. Variation of channel parameters in the range given here has negligible effect on the further evolution of the flowfield. Because at this time the gas/plasma has not moved much, the density is assumed to be that at atmospheric level. Pressure in the channel is calculated from these values of density and temperature. Flow velocity is taken to be zero everywhere in domain of computation at initial time. The temperature is distributed smoothly (decreasing exponentially) in and around the channel such that it is equal to room temperature at a point two channel radii away from the axis of symmetry. The initial distribution of the primitive variables is cylindrically symmetric.

Boundary Conditions

The boundary AA' is symmetrical, i.e., here $u = 0$, and the radial component of the space gradient of all dependent variables vanishes. The boundaries $ABCD$, $A'B'C'D'$ in case I and ABD, $A'B'D'$ in case II are treated as slip walls serving as an infinite heat sink. The normal (to the surface) component of velocity is assumed to be zero on these boundaries, and the temperature inside the electrodes is kept at 300 K by introducing a grid line inside electrodes. The grid points inside the electrodes are used only to calculate the heat flux directed into the electrodes. Further, the gradient of specific internal energy and density is assumed zero to calculate these quantities at the boundary points. The boundaries DE, $D'E'$, and EE' are treated as far-field boundaries, i.e., the normal component of space gradient of all dependent variables at the boundary under consideration vanishes.

Numerical Scheme

Let $U^n_{i,j}$ denote the value of U at the space point (r_i, z_j) in the rz plane and the time level t^n. Now, given the values $U^n_{i,j}$ at the n time level, the solution at a higher time level is calculated with the following scheme:

$$U^{n+2}_{i,j} = L_r(\Delta t_r)L_z(\Delta t_z)L_z(\Delta t_z)L_r(\Delta t_r)U^n_{i,j} \tag{28}$$

The operators $L_r(\Delta t_r)$ and $L_z(\Delta t_z)$ are one-dimensional two-step predictor–corrector difference operators corresponding to the MacCormack scheme. $L_r(\Delta t_r)$ is defined by $U^{**}_{i,j} = L_r(\Delta t_r)U^*_{i,j}$, such that

$$U^*_{i,j} = U^*_{i,j} - (\Delta t_r/\Delta r)\left(G^*_{i+1,j} + S^*_{i+1,j} - G^*_{i,j} - S^*_{i,j}\right) - \Delta t_r \Phi^*_{i,j} \tag{29}$$

$$U^{**}_{i,j} = \tfrac{1}{2}\left[U^*_{i,j} + U^{\bar{*}}_{i,j} - (\Delta t_r/\Delta r) \times \left(G^{\bar{*}}_{i,j} + S^{\bar{*}}_{i,j} - G^{\bar{*}}_{i-1,j} - S^{\bar{*}}_{i-1,j}\right) - \Delta t_r \Phi^{\bar{*}}_{i,j}\right] \tag{30}$$

where

$$S^*_{i,j} = a\left[\left(|u^*_{i,j}| + c^*_{i,j}\right) \times \frac{\left|\left(p^*_{i+1,j} - 2p^*_{i,j} + p^*_{i-1,j}\right)\right|}{\left(p^*_{i+1,j} + 2p^*_{i,j} + p^*_{i-1,j}\right)}\left(U^*_{i,j} - U^*_{i-1,j}\right)\right]$$

$$S^{\bar{*}}_{i,j} = a\left[\left(|u^{\bar{*}}_{i,j}| + c^{\bar{*}}_{i,j}\right) \times \frac{\left|\left(p^{\bar{*}}_{i+1,j} - 2p^{\bar{*}}_{i,j} + p^{\bar{*}}_{i-1,j}\right)\right|}{\left(p^{\bar{*}}_{i+1,j} + 2p^{\bar{*}}_{i,j} + p^{\bar{*}}_{i-1,j}\right)}\left(U^{\bar{*}}_{i+1,j} - U^{\bar{*}}_{i,j}\right)\right]$$

Similarly, the operator $L_z(\Delta t_z)$ is defined by $U^{**}_{i,j} = L_z(\Delta t_z)U^*_{i,j}$, such that

$$U^{\bar{*}}_{i,j} = U^*_{i,j} - (\Delta t_z/\Delta z)\left(H^*_{i,j+1} + \Sigma^*_{i,j+1} - H^*_{i,j} - \Sigma^*_{i,j}\right)$$

$$U^{**}_{i,j} = \tfrac{1}{2}\left[U^*_{i,j} + U^{\bar{*}}_{i,j} - (\Delta t_z/\Delta z)\left(H^{\bar{*}}_{i,j} + \Sigma^{\bar{*}}_{i,j} - H^{\bar{*}}_{i,j-1} - \Sigma^{\bar{*}}_{i,j-1}\right)\right]$$

where

$$\Sigma^*_{i,j} =$$

$$a\left[(|w^*_{i,j}| + c^*_{i,j})\frac{|(p^*_{i,j+1} - 2p^*_{i,j} + p^*_{i,j-1})|}{(p^*_{i,j+1} + 2p^*_{i,j} + p^*_{i,j-1})}(U^*_{i,j} - U^*_{i,j-1})\right]$$

$$\Sigma^{\bar{*}}_{i,j} =$$

$$a\left[(|w^{\bar{*}}_{i,j}| + c^{\bar{*}}_{i,j})\frac{|(p^{\bar{*}}_{i,j+1} - 2p^{\bar{*}}_{i,j} + p^{\bar{*}}_{i,j-1})|}{(p^{\bar{*}}_{i,j+1} + 2p^{\bar{*}}_{i,j} + p^{\bar{*}}_{i,j-1})}(U^{\bar{*}}_{i,j+1} - U^{\bar{*}}_{i,j})\right]$$

An additional heat-loss term for electrodes, derived from Fourier law, is added to the operators while operating on a grid point adjacent to the electrode surface.

To maintain the truncation error uniform near the boundaries, the order of differencing is switched over in predictor–corrector after every two time cycles. To maintain the order of accuracy of the scheme, special care has been taken in evaluating fluxes G, H, and the source term Φ. The derivatives appearing within G or H are replaced by the differences opposite to those used for the derivatives of G or H themselves. For example, in the case when $(\partial G/\partial r)$ is replaced by forward difference, the term $h_r[\equiv -\kappa(\partial\theta/\partial r)]$ appearing in G has to be replaced by backward difference, and vice versa. The differential operators appearing in Φ are replaced by difference operators having the same order of differencing as for replacing $\partial G/\partial r$.

The phoenical type of FCT (Ref. 12) is applied in the same space direction just after the application of the respective operator in that direction. Special care is taken to calculate diffusive and antidiffusive fluxes in the z direction close to the electrodes. During computation, it is ensured that the heat flux is always directed toward the electrode surface in the grid line adjacent to it.

The time steps Δt_r and Δt_z are calculated independently from Courant–Friedrichs–Lewy (CFL) stability criterion in the radial and axial directions. To make the operator symmetric in Eq. (28), we choose the time step Δt such that

$$\Delta t = \min(\Delta t_r, \Delta t_z) \tag{31}$$

The space mesh size is the same in both r and z directions. The minimum mesh size was about 0.05 × 0.05 mm. The time step corresponding to this mesh was about 1 ns at the time of peak power input. It increases at later stages.

Given the initial condition, the solution at a higher time level is obtained by applying the difference operators L_r and L_z in the sequence prescribed by Eq. (28). First, consider the application of L_r. Solution at a higher time level is predicted by the use of Eq. (29). Temperature and pressure are calculated from predicted values of specific internal energy and mass density, using state equations (11) and (12). Equation (12) is nonlinear in temperature and is solved numerically using the method of false positions. An appropriate solution interval for temperature is estimated from the temperature at the previous time level and the application of the mean-value theorem from mathematical analysis. The temperature and density values are then used to calculate joule heating and radiative losses at a predicted level. Now, the solution is corrected with Eq. (30). The phoenical type of FCT is applied in the r direction over the corrected solution with the help of the solution at the previous time level. Temperature and pressure are calculated at the corrected level, as stated above. This completes the application of the operator L_r. Other operators are applied in a similar manner, using the appropriate corresponding equations.

The accuracy of the numerical scheme is checked by the standard procedure of mesh refinement. No significant dissimilarities regarding amplitude and speed of the shock wave are observed when mesh size in both directions is reduced by half.

Results and Discussion

The experimental results reported by Borghese et al.[13] are used to compare with the model (case I). The electrical current measured is used in the calculations as input. The spark gap is 2 mm, and air is used instead of nitrogen. The electrode geometry is slightly different in the experiment as compared to case I. Figure 2 shows the normalized waveforms of the spark voltage (GV), electric current (j), and joule energy (Ej) as a function of time, along with their maximum values compared to the measured values. The time history of the calculated waveforms fairly matches with the experiment; however, the absolute maximum values differ slightly. The model gives 12 mJ as the gap energy compared to 14 mJ, and 16 kV as the gap voltage compared to 12 kV.

The mass density in the equatorial plane at 5 and 10 μs is compared with experimental values in Fig. 3. The wave position is fairly close. The difference in the two distributions behind the wave might be because of the difference of electrode geometry. Later, we see that this influence is quite strong.

Calculations show that in both cases of electrode geometry the shock wave starts separating from plasma kernel at about 0.5μs and at 2 μs it has left the plasma kernel far behind (Fig. 4). The velocity field at the same time is plotted in Fig. 5, where the flow ahead of the wave is undisturbed. The wave emerges out of the gap grazing over the surface, facing sudden expansion (for case II) in the z direction, in which the momentum of the gas is almost zero. A rarefaction wave is generated, causing a backflow into the gap. This rarefaction effect is stronger in case II than in case I, where the slanting surface of the electrodes has provided gradual expansion. The loss of shock overpressure can be seen near the electrodes. The maximum pressure in the wave front is around the $z = 0$ line and decreases gradually as we move along the wave front toward the electrodes.

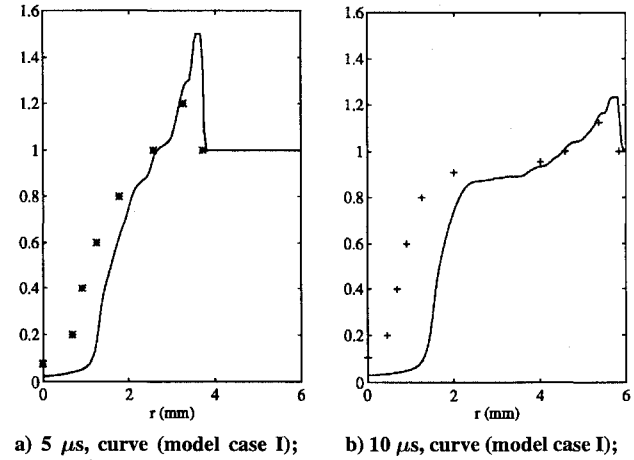

a) 5 μs, curve (model case I); *, experiment

b) 10 μs, curve (model case I); +, experiment

Fig. 3 Comparison of scaled (with atmospheric value) mass density with experiment.

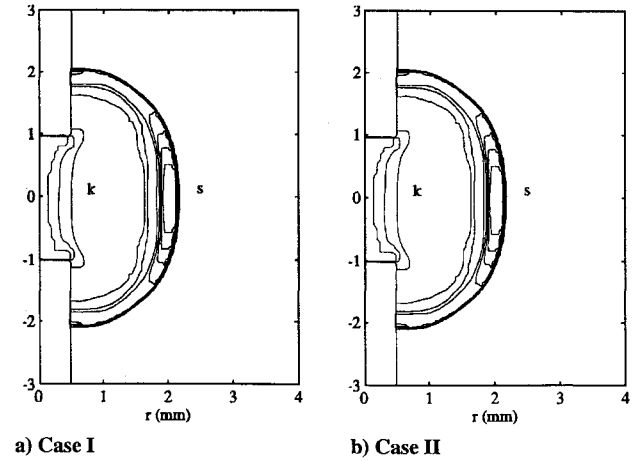

a) Case I

b) Case II

Fig. 4 Plasma kernel k and shock wave s at 2 μs for 2-mm spark gap. The plasma kernel is plotted as isotherms and the shock wave as isobars, both in the rz plane. Empty spaces on upper and lower left corners marked with a boundary line are electrodes.

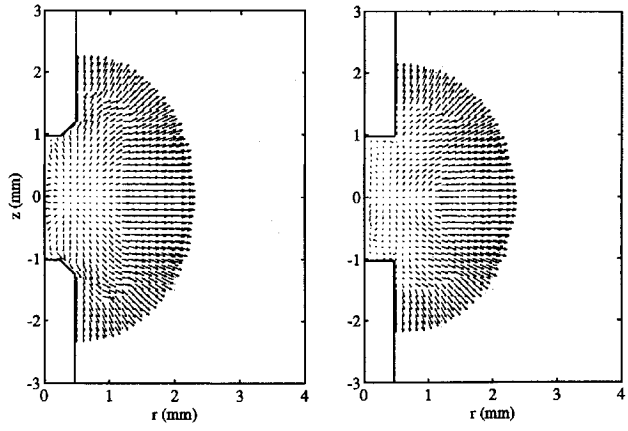

a) Case I b) Case II

Fig. 5 Velocity vector field at 2 μs for 2-mm spark gap.

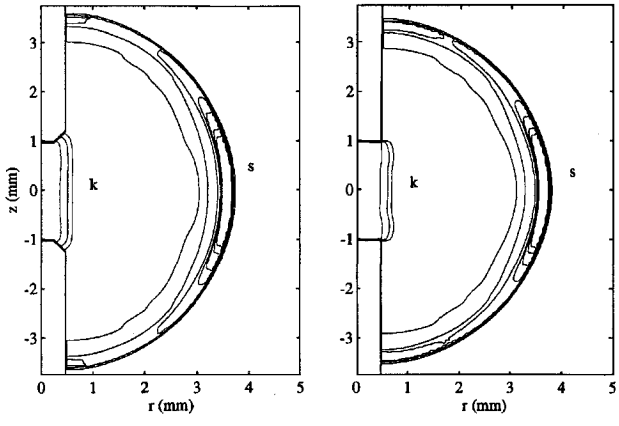

a) Case I b) Case II

Fig. 6 Plasma kernel k and shock wave s at 5 μs for 2-mm spark gap. The plasma kernel is plotted as isotherms, and the shock wave as isobars, both in the rz plane. Empty spaces on upper and lower left corners marked with a boundary line are electrodes.

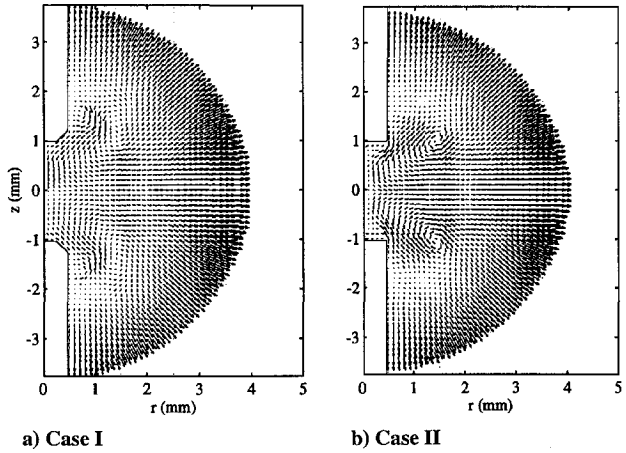

a) Case I b) Case II

Fig. 7 Velocity field at 5 μs in the rz plane.

At 5 μs, the electric current has already gone down, and the electrical conductivity of the gap is high enough, which means that inflow of energy has ceased. The flow of cold gas toward (into) the gap has nearly stopped the expansion of the plasma kernel, but the shock wave is still expanding at quite high speed, as can be seen in Figs. 6 and 7. Two pairs of vortices in case I and one pair of vortices in case II have been formed near the gap, rotating in the opposite direction, bringing cooler gas into the gap (see Fig. 7). In both cases, a galaxy of small vortices is spread along the shock-wave front, indicating the distinct shock structure and rather complicated

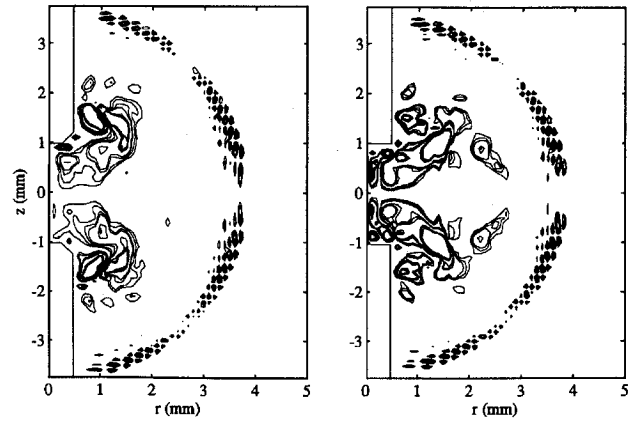

a) Case I b) Case II

Fig. 8 Vortex lines at 5 μs in the rz plane for 2-mm spark gap.

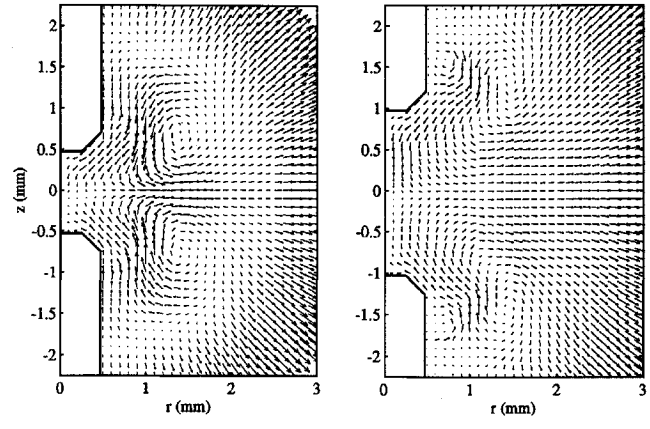

a) 1-mm spark gap b) 2-mm spark gap

Fig. 9 Velocity field at 5 μs in the rz plane. In both plots, electrodes of case I are used.

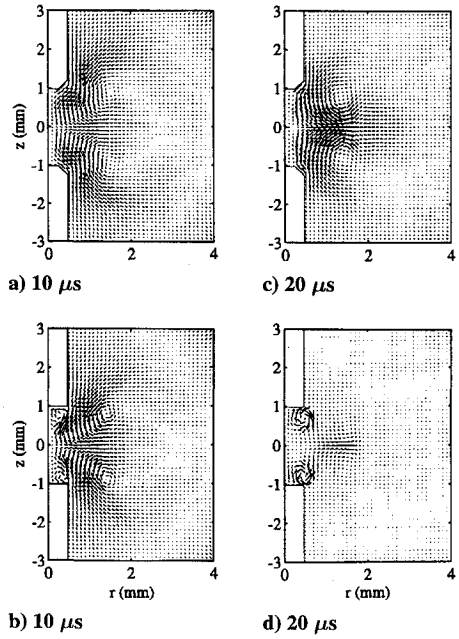

a) 10 μs c) 20 μs

b) 10 μs d) 20 μs

Fig. 10 Velocity field at different times in the rz plane.

flow through the shock surface (Fig. 8). The influence of spark gap is studied by decreasing the gap for case I from 2 to 1 mm and solving for the same power input. The flowfield given in Fig. 9 shows that the vortex structure has changed, giving stronger mixing compared to the 2 mm gap with the same geometry. The number of vortices is reduced to two, and they have moved closer to the $z = 0$ line.

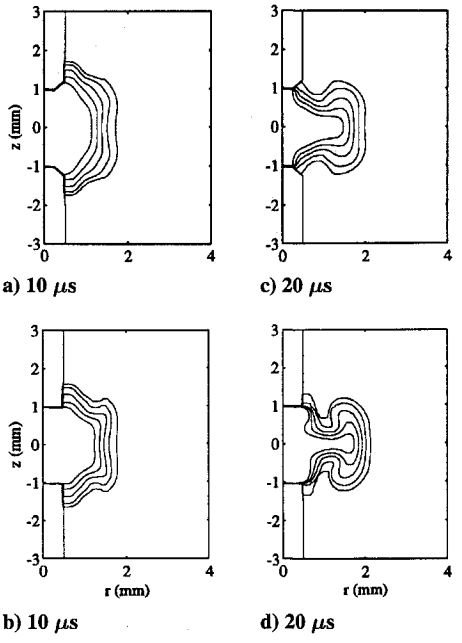

Fig. 11 Isotherms corresponding to 500, 1000, 2000, 3000, and 4000 K (from outside to inside) for 2-mm spark gap in the rz plane.

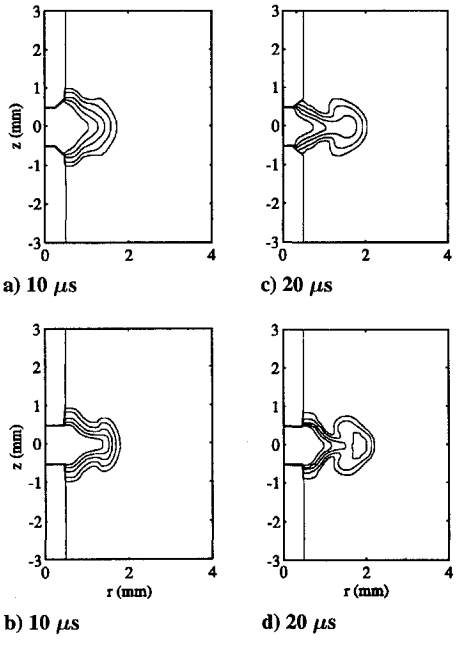

Fig. 12 Isotherms corresponding to 500, 1000, 2000, 3000, and 4000 K (from outside to inside) for 1-mm spark gap in the rz plane.

About 7 μs after the onset of spark, the shock wave has lost most of its amplitude and the temperature rise in the gas attributable to shock compression is about 20 K. Although at later times the shock position is quite similar in both cases, the overpressure is different. At the same time, the shock wave with an average overpressure of about 1.5 bar is about to leave the domain of computation. The computations are carried out up to 40 μs in the same space domain to study the evolution of the plasma kernel. Note that far-field boundary conditions do not affect the flowfield near the electrodes. The pressure is almost atmospheric, and a situation of free expansion or generation of a rarefaction wave at outer boundaries does not arise in this case.

After 10 μs, the two cases under consideration exhibit their distinct flow patterns. At 10 and 20 μs, the velocity field for the two cases is given in Fig. 10. At 10 μs, in case I, we see one pair of vortices near electrodes but out of the gap and away from the $z = 0$ line (Fig. 10a). On the other hand, for case II, two distinct pairs of

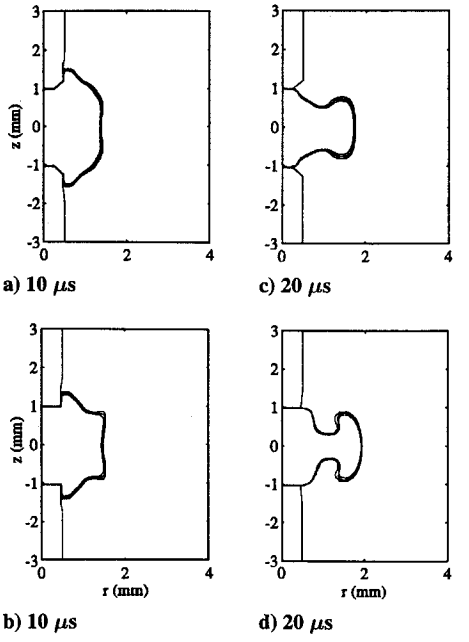

Fig. 13 Isotherms corresponding to 1800, 2000, and 2200 K (from outside to inside) for 2-mm spark gap in the rz plane.

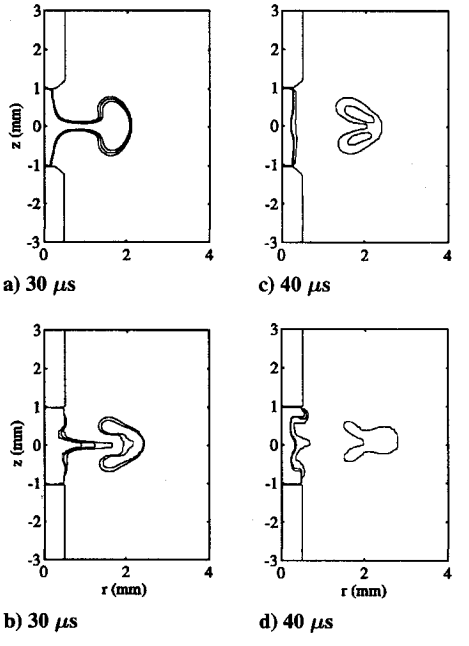

Fig. 14 Isotherms corresponding to 1800, 2000, and 2200 K (from outside to inside) for 2-mm spark gap in the rz plane.

vortices, one inside the gap near the electrodes and the other outside the gap near the $z = 0$ line (Fig. 10b). This complicated flow pattern is retained by the plasma (see Figs. 10c and 10d) and is going to shape the plasma kernel at later stages. Because the power input to both cases is the same, one can associate this feature of the flow with the electrode geometry.

The in-flowing cold gas from outside the gap mixes with the hotter gas in the gap and then is thrown out by the vortices rotating in the opposite directions. Moreover, by this time, heat-conductive processes influence their neighbors. The resulting mixture at slightly lower temperature than at 5 μs starts growing. Figure 11 shows the isotherms for the two cases at 10 and 20 μs. The kernel in case II is taking the shape of a torus with a deep groove on the outer surface at 20 μs. Isotherms corresponding to the same levels as those shown in Fig. 11 are given for the same electrode geometry, in Fig. 12, but the spark gap is reduced to 1 mm. In this situation at 20 μs, for case II the kernel has a spheroidal hot bubble wrapped in relatively cooler gas, whereas for case I such an isolated hot bubble cannot

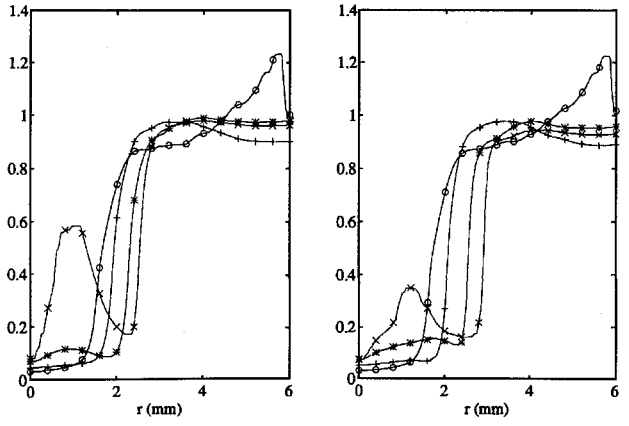

a) Case I b) Case II

Fig. 15 Radial distribution of calculated scaled (with atmospheric value) mass density along the $z = 0$ line at different times: $\circ$, 10 μs; $+$, 20 μs; $*$, 30 μs; and $\times$ 40 μs.

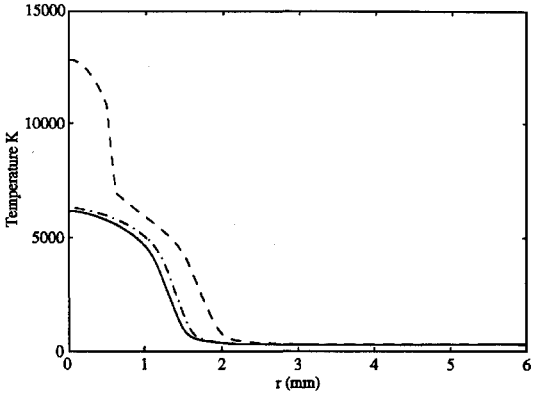

Fig. 16 Temperature (K) vs radial coordinate (mm) at 10 μs. Solid and chain curves (this model, cases I and II, respectively) at $z = 0$ line (dashed curve = one-dimensional model with same power input as used here).

be seen (Fig. 12). No doubt, a groove on the outer surface has appeared, which is growing with time; there is a tendency for such a phenomenon to occur but a look at the vortex structure shows that it is relatively slow compared to case II.

The most likely temperature from the ignition aspect is around 1800–2100 K. To study the gas heating in this temperature range, isotherms are plotted at 10, 20, 30, and 40 μs for the two cases in Figs. 13 and 14. The influence of the geometry in heating the gas is well pronounced. In case II, a hot bubble engulfed by cooler gas has been formed at 30 μs. A larger volume of the gas is heated to the said temperature range in case I.

Scaled mass density in the equatorial plane at 10, 20, 30, and 40 μs for the two cases under consideration is plotted against r in Fig. 15. The density on and very close to the axis of the spark has not yet returned to its normal value as given in the above experiment during this time regime, but one sees the tendency that it is going to do so later.

At early stages, the heat loss to the electrodes seems to be insignificant if one looks at the isotherms, but this is not true. The heat loss to the electrodes and the convective cooling by the recirculation of the gas in the gap is compared to a one-dimensional cylindrically symmetrical model[5] with no heat loss to the electrodes at 10 μs in Fig. 16. The temperature at the $z = 0$ line from these calculations is plotted against r. This indicates that heat loss to the electrodes at later stages of the discharge is significant.

Concluding Remarks

In this paper the energy input into chemically inert gas and the flowfield generated by an ultrafast electrical spark discharge during the early phase (10 ns–40 μs) of its evolution is studied. It is observed that the flow structure developed at the early stages more or less prevails at later stages and strongly influences the shape and evolution of the hot kernel. The electrode geometry and the electrode configuration are responsible for the development of flow structure. The strength of vortices generated in the flowfield is influenced by the power input to the gap, and their location of emergence is dictated by the electrode shape and configuration. The heat transfer after 2 μs is dominated by convective diffusion.

The strong mixing produced by hydrodynamic effects and the electrode geometry give the indication that the magnetic pinch effect is negligible. The model presented here can produce a realistic initial condition for the study of ignition processes in combustible mixtures, for example, in the internal combustion engine.

Acknowledgments

The author is indebted to E. Lundgren for his cooperation and suggestions throughout the course of this work. Particular mention should be made of the help of C. Fureby and S.-I. Möller in the graphic presentation of the work.

References

[1]Chomiak, J., "Flame Development from an Ignition Kernel in Laminar and Turbulent Homogeneous Mixtures," *17th Symposium (International) on Combustion*, Combustion Inst., Pittsburgh, PA, 1979, pp. 255–263.

[2]Haley, R. F., and Smy, P. R., "Electrically Induced Turbulence—the Short Duration Spark," *Journal of Physics D: Applied Physics*, Vol. 22, No. 2, 1989, pp. 258–265.

[3]Kono, M., Niu, K., Tsukamoto, T., and Ujie, Y., "Mechanism of Flame Kernel Formation Produced by Short Duration Sparks," *22nd Symposium (International) on Combustion*, Combustion Inst., Pittsburgh, PA, 1988, pp. 1643–1649.

[4]Maly, R., and Vogel, M., "Initiation and Propagation of Flame Fronts in Lean CH_4–Air Mixtures by the Three Modes of the Ignition Spark," *17th Symposium (International) on Combustion*, Combustion Inst., Pittsburgh, PA, 1979, pp. 821–831.

[5]Akram, M., "Continuum Mechanical Models for Spark Discharge Simulation," Thesis (TeknL), Div. of Mechanics, Lund Inst. of Technology, Lund, Sweden, 1991.

[6]Serrin, J., "Mathematical Principles of Classical Fluid Mechanics," *Encyclopedia of Physics*, Vol. 8, Pt. 1, *Fluid Dynamics I*, Springer–Verlag, Berlin, 1959, pp. 125–263.

[7]Plooster, M. N., "Shock Waves from Line Sources. Numerical Solution and Experimental Measurements," *Physics of Fluids*, Vol 13, No. 11, 1970, pp. 2665–2675.

[8]Pai, S.-I., *Radiation Gas Dynamics*, Springer–Verlag, Berlin, 1966.

[9]Sher, E., and Keck, J. C., "Spark Ignition of Combustible Gas Mixtures," *Combustion and Flame*, Vol. 66, No. 1, 1986, pp. 17–25.

[10]Anderson, D. A., and Pletcher, R. H., *Computational Fluid Mechanics and Heat Transfer*, Hemisphere, New York, 1984.

[11]MacCormack, R. W., "Numerical Solution of the Interaction of a Shock Wave with a Laminar Boundary Layer," *Lecture Notes in Physics*, Vol. 8, edited by M. Holt, Springer–Verlag, Berlin, 1971, pp. 151–163.

[12]Fletcher, C. A. J., *Computational Techniques for Fluid Dynamics, Vol 2. Specific Techniques for Different Flow Categories*, 2nd ed., Springer–Verlag, Berlin, 1991.

[13]Borghese, A., D'Alessio, A., Diana, M., and Venitozzi, C., "Development of Hot Nitrogen Kernel, Produced by a Very Fast Spark Discharge," *22nd Symposium (International) on Combustion*, Combustion Inst., Pittsburgh, PA, 1988, pp. 1651–1659.